Lamellar microstructure of emulsions

By VITTORIO CRISTINI[1] †‡, M. SIMEONE[2], S. GUIDO[2], R. HOOPER[1] AND C. W. MACOSKO[1]

[1]Department of Chemical Engineering and Materials Science, University of Minnesota, 421 Washington Avenue S.E., Minneapolis, MN 55455, USA

[2]Dipartimento di Ingegneria Chimica, Universita' degli Studi di Napoli "Federico II", Piazzale V. Tecchio 80, 80125 Napoli, Italy

(Received ?? and in revised form ??)

Transient three-dimensional drop deformation is studied in dilute emulsions for large capillary numbers Ca, corresponding to strong-flow or low-interfacial-tension conditions. Steady, planar linear flows are considered, described by the dimensionless vorticity β orthogonal to the plane of flow. For drop-to-matrix viscosity ratios $\lambda < 1$, drops widen along the vorticity direction due to the compressional component of the imposed flow. The drops are strongly elongated by the flow, and thus assume flat lamellar configurations, leading to remarkable interfacial area generation.

We analyze the limit $Ca \to \infty$ first, and present analytic results demonstrating that in this case drop deformation is described by a universal function of λ, independent of the vorticity β. Rigid-body rotation merely affects the time-evolution, i.e., with increasing β, drops are more rotated away from the extensional direction of the flow thereby delaying deformation. We provide an exact solution that describes drop deformation far from the initial conditions. A constant drop width is achieved along the direction of vorticity, leading to the development of a stable lamellar morphology.

To explore the effect of interfacial tension (finite Ca), drop evolution is then calculated using adaptive boundary-integral simulations and measured using video-microscopy. The experiments and the simulations are always found to be in good agreement. The extent of drop widening and interfacial area generation is strongly affected by a small but finite interfacial tension. Widening occurs only above a minimum capillary number, which increases with the viscosity ratio λ and the vorticity β. The persistence of lamellar configurations is examined. As drops lengthen and flatten, local capillarity associated with high surface curvatures eventually becomes effective, and widening disappears. The development of a lamellar microstructure is thus a transitory phenomenon at finite capillary numbers: flattened drops evolve into slender cylindrical threads of fluid that finally break up.

1. Introduction

Immiscible polymer blends are typically composed of droplets of one phase dispersed in a polymeric matrix and often exhibit synergetic features that are used to produce plastics and elastomers with optimal properties (Utracki 1991). Under strong flow processing conditions, or when interfacial tension is small (such as in the presence of block-copolymers at the interfaces), polymer blends can assume lamellar microstructures characterized by

† Also at the School of Mathematics, University of Minnesota
‡ Corresponding author. E-mail: cristini@cems.umn.edu

remarkable elongation and flattening of the droplets. It has been shown that such blend microstructures can reduce by orders of magnitude the permeability of polyethylene to hydrocarbons (Subramanian 1985), and of extruded polypropylene sheets (Lohfink & Kamal 1993) and polyethylene blown films (Lee & Kim 1996) to oxygen, and can increase the impact strength of high density polyethylene (Yuan, Friedrich & Karger-Kocsis 1994). Low permeability, good mechanical properties and low cost make it desirable to employ such morphologies in the fabrication of diffusion barriers useful for such applications as gasoline tanks (Subramanian & Plotzker 2000).

Typically such blends are processed by melt mixing followed by extrusion and then rapid quenching. Heuristic strategies have been employed during emulsification, such as the use of mild mixing (Subramanian 1984, 1985; Subramanian & Mehra 1987; Garmabi & Kamal 1997), because it produces larger drops of the dispersed phase that deform into lamellae of larger interfacial area without breaking during extrusion of the melt. The key to creating lamellae with desired morphology is a quantitative understanding of the transient deformation of viscous and viscoelastic drops under high-capillary-number conditions.

Industrial applications like these have stirred recent interest in studying large drop deformations in the strong-flow (or low-surface-tension) limit. At present however few studies are available in the literature for this regime. Morphological changes under transient shear have been studied using rheology and light scattering (Vinckier, Moldenaers & Mewis 1996, 1997; Vinckier, Mewis & Moldenaers 1997), to estimate the change in drop aspect ratio (Sondergaard & Lyngaae-Jorgenson 1996). Direct visualizations of transient drop deformation in shear flow are available for viscous and slightly non-Newtonian systems (Yamane *et al.* 1998). Delaby *et al.* (1994), Delaby, Ernst & Muller (1995), and more recently Saito & Macosko (1998) have followed drop evolution in uniaxial extension by freezing samples and then examining them under a microscope. Images of viscoelastic drop deformation in strong shear flows have been obtained by Levitt, Macosko & Pearson (1996) and by Jeon & Macosko (2000), using a counter-rotating apparatus. The images reveal $O(1)$ widening of the drops in the vorticity direction and a remarkable interfacial-area generation for drop-to-matrix viscosity ratios less than 1. Some theoretical studies have recently been presented. Maffettone & Minale (1998) described drop deformation assuming ellipsoidal drop shapes. Wetzel & Tucker (2001) presented a study valid in the limit of zero interfacial tension and Newtonian fluids under Stokes flow conditions; the transient drop deformation predicted by their theory is in quantitative agreement with experimental observations (Comas-Cardona & Tucker 2001) of drops with no interfacial tension. The theory developed by Wetzel & Tucker (2001) predicts $O(1)$ stable widening of drops for viscosity ratios less than 1, revealing that the phenomenon of widening and lamellae formation is of Newtonian origin.

In this paper, we present a comprehensive investigation of transient drop deformation before breakup, in planar flows with rotation for capillary numbers $Ca > 1$. Our results apply to dilute Newtonian emulsions under low-Reynolds-number conditions. In melt-mixing devices, the Reynolds number based on the drop scale is typically very small. Although polymeric fluids exhibit viscoelastic behavior in general, the phenomenon of widening and lamellae formation is of Newtonian origin, as demonstrated in this paper using the theory developed by Wetzel & Tucker (2001), and is only quantitatively affected by elastic stresses. The results of our study can be directly employed in the production of lamellar blends with desired properties. In our investigation, adaptive boundary-integral simulations (Cristini, Bławzdziewicz & Loewenberg 1998, 2001), capable of describing large deformations, are used. For simple shear flow, experimental measurements of drop deformation are provided using the video-microscopy apparatus developed by Guido &

Villone (1998). The special case of zero interfacial tension is studied extending the theory developed by Wetzel & Tucker (2001).

In §2 the assumptions of our study are stated, and scaling arguments relevant to the evolution of lamellar microstructures are discussed. In §3 an exact equation describing drop deformation and widening for zero interfacial tension and an asymptotic solution are presented. Our experimental and numerical techniques are described in §4, and transient drop deformation at finite capillary numbers is investigated and compared to the analytic results using experiments and boundary-integral simulations in §5. Concluding remarks and directions of future work are given in §6.

2. Assumptions and scaling arguments

We consider a dilute emulsion of droplets such that hydrodynamic interactions are negligible. We therefore focus on a single drop of volume $\frac{4}{3}\pi {R_0}^3$, density $\hat{\rho}$ and viscosity $\hat{\mu}$ in an unbounded fluid of density ρ and viscosity μ. The drop surface is surfactant-free, and no temperature gradients are present, so that the interfacial tension σ is constant. Also, buoyancy effects are neglected. All assumptions are satisfactorily met in our experiments (cfr. §4.1).

The external fluid undergoes a steady planar linear flow, impulsively started at time $t = 0$. The drop is initially spherical and remains centered at the origin of the reference system during deformation. The imposed velocity field has the form

$$\mathbf{v}^{\infty} = \dot{\gamma}(\mathbf{E} + \beta\mathbf{\Omega}) \cdot \mathbf{x}, \tag{2.1}$$

where $\dot{\gamma}$ is the magnitude of the rate of strain, $\mathbf{E}$ and $\mathbf{\Omega}$ are the dimensionless rate-of-strain and vorticity tensors, respectively. The only non-zero components of the velocity gradient are

$$E_{xy} = E_{yx} = 1/2 \quad \text{and} \quad \Omega_{xy} = -\Omega_{yx} = 1/2,$$

which define flows in the xy-plane and vorticity in the z-direction. The dimensionless vorticity β characterizes the type of flow and includes the important cases of shear flow ($\beta = 1$) and hyperbolic flow ($\beta = 0$). According to notation (2.1), the imposed strain is given by $\dot{\gamma}t$ for shear flow.

We consider flow and fluid conditions for which the Reynolds number based on the drop size is low and therefore apply the Stokes equations to describe the fluid motion. It follows (Kim & Karrila 1991) that the relevant parameters for drop deformation are the capillary number

$$Ca = \tau_{\sigma}/\tau_{\dot{\gamma}}, \tag{2.2}$$

which is the ratio of the capillary relaxation time $\tau_{\sigma} = \mu R_0/\sigma$ to the flow time $\tau_{\dot{\gamma}} = \dot{\gamma}^{-1}$, the viscosity ratio $\lambda = \hat{\mu}/\mu$, and the dimensionless vorticity β.

In the following, the drop shape is characterized by the normalized length (maximum dimension) R_1/R_0 and thickness R_2/R_0, both in the plane xy of the flow, and by the width R_3/R_0, along the vorticity direction z. Note that at time $t = 0$ we have $R_1 = R_2 = R_3 = R_0$. To quantify interfacial area generation during drop deformation we use

$$R_1 R_3/R_0^2,$$

which is a projection of the drop image onto an equivalent ellipse in the xz-plane. This corresponds to viewing the drop along the y-axis.

2.1. *Lamellar microstructure*

Under conditions of $0 \leq \beta \leq 1$ and $Ca > O(1)$, no stationary configurations exist (Stone 1994), and drop deformation from spherical in a steady flow (2.1) is characterized by unbounded elongation:

$$R_1/R_0 \to \infty \quad \text{as} \quad t \to \infty, \tag{2.3}$$

and ultimately leads to breakup. In this work, the transient microstructure preceding breakup is described. For viscosity ratios $\lambda < 1$, drops widen while elongating in the flow:

$$R_3/R_0 \geq 1. \tag{2.4}$$

From conservation of volume, drop widening results in large projected area generation

$$R_1 R_3/R_0^2 \sim R_1/R_0, \tag{2.5}$$

and enhances the development of lamellar microstructures.

In the presence of a finite interfacial tension (finite Ca), drops maintain an $O(1)$ width only until local capillarity becomes important. At this point transient widening disappears, and drops develop a cylindrical configuration characterized by a circular neck connecting bulbous ends. Capillarity drives the neck smaller and finally leads to a series of breakup events that disintegrate the drop into a number of fragments. The breakup events and the resulting size distributions have been studied in detail (Marks 1999; Cristini *et al.* 2001; Renardy & Cristini 2001a,b). Capillarity leads to the scaling $R_3/R_0 \approx R_2/R_0 \sim (R_1/R_0)^{-\frac{1}{2}}$, which corresponds to an area generation

$$R_1 R_3/R_0^2 \sim (R_1/R_0)^{\frac{1}{2}} \tag{2.6}$$

that is smaller than (2.5), and grows weakly as $R_1/R_0 \to \infty$. For $\lambda > 1$ no widening occurs, and other modes of deformation, (e.g., tumbling) are possible (Wetzel & Tucker 2001), which we will not investigate here.

3. Analytic results for $Ca \to \infty$

3.1. *Summary of evolution equations*

Wetzel & Tucker (2001) formulated a theory for drop deformation valid in the limit $Ca \to \infty$. They recast the Stokes equations combined with boundary conditions characteristic of a fluid-fluid interface with no surface tension into an evolution equation, which we rewrite as:

$$\frac{\mathrm{d}\mathbf{A}}{\mathrm{d}t} = 2\dot{\gamma}\, \hat{\mathbf{S}}\{\mathbf{A} \cdot (\beta\boldsymbol{\Omega} + (\mathbf{B} + \mathbf{C}) : \mathbf{E})\}, \tag{3.1}$$

for the special case of a planar flow (2.1). Here, drop shape and drop orientation are described by the tensor $\mathbf{A}$, from the result that an initially ellipsoidal isolated drop in an infinite fluid undergoing a general linear flow evolves into an ellipsoid:

$$\mathbf{x} \cdot \mathbf{A} \cdot \mathbf{x} = 1. \tag{3.2}$$

In (3.1) operator $\hat{\mathbf{S}}\{...\}$ takes the symmetric part, and time-dependent fourth-order tensors $\mathbf{B}$ and $\mathbf{C}$ are functions of the axes R_i/R_0 of the ellipsoid, its orientation, and the viscosity ratio λ. Following Wetzel & Tucker (2001), we define the axis ratios

$$C = R_2/R_1 \quad \text{and} \quad D = R_2/R_3. \tag{3.3}$$

Note that from conservation of volume, $R_1 R_2 R_3 = R_0^3$ identically so that the axis ratios C and D completely define the ellipsoidal drop shape. Note also that corresponding to

the planar flow (2.1) the orientation of the ellipsoid is completely defined by an angle θ between the direction of R_1–axis and the x–axis, i.e. $\theta = 0$ and $\pi/2$ on the positive x– and y–axis, respectively. Thus tensor $\mathbf{B} = \mathbf{B}(C, D, \theta, \lambda)$ and the same functional dependence applies to $\mathbf{C}$.†

We use the definitions

$$A^*_{ij} = \begin{cases} (R_i/R_0)^{-2}, & i = j \\ 0, & i \neq j \end{cases} \tag{3.4}$$

where the "*" denotes components in the *ellipsoid reference system*, defined by the directions of R_1, R_2, R_3, that are related to the xyz–frame by a rotation θ around the z–axis. We also denote by B^*_{ij} the components (in contracted notation) of $\mathbf{B}$ in the ellipsoid reference frame. The components B^*_{ij} are given by Wetzel & Tucker (2001) by complicated formulas involving elliptic integrals, as functions of the axis ratios C and D and viscosity ratio λ, but *independent* of the dimensionless vorticity β:

$$B^*_{ij} = B^*_{ij}(C, D, \lambda), \quad i, j = 1, 6. \tag{3.5}$$

Note that indices 2 and 3 for components of $\mathbf{B}$ in contracted notation are switched with respect to Wetzel & Tucker (2001) for consistency with the usual notation in the experimental literature.

3.2. *Exact equation for drop shape*

We derived an exact equation for the drop shape by eliminating time t from equations (3.1)–(3.2) with (3.4), since the derivation is more easily performed using the axes R_i rather than the axis ratios C, D. We obtain, after algebraic manipulations that involve rotation of tensors by an angle θ,

$$\begin{aligned} \frac{\mathrm{d}(R_1^{-2} + R_2^{-2})}{\mathrm{d}t} &= 2\dot{\gamma}\ \left(R_2^{-2}(B^*_{22} - B^*_{21}) + R_1^{-2}(B^*_{12} - B^*_{11})\right)\ \sin(2\theta) \\ \frac{\mathrm{d}R_3^{-2}}{\mathrm{d}t} &= -2\dot{\gamma}\ R_3^{-2}(B^*_{31} - B^*_{32})\ \sin(2\theta). \end{aligned} \tag{3.6}$$

By dividing the two equations (3.6) to eliminate time t, the time dependent rotation angle θ (which depends on β) is eliminated. By introducing definitions (3.3) for C and D, and after further manipulations that involve properties of the B^*_{ij} provided by Wetzel & Tucker (2001), we obtain

$$\frac{D}{C} \cdot \frac{\mathrm{d}C}{\mathrm{d}D} = \frac{B^*_{21} - B^*_{22} - B^*_{11} + B^*_{12}}{B^*_{21} - B^*_{22} - B^*_{31} + B^*_{32}}. \tag{3.7}$$

Equations (3.5) and (3.7) reveal that in planar flows the drop shape is described by a universal scalar function

$$f(C, D, \lambda) = 0, \tag{3.8}$$

which satisfies (3.7) and is independent of the vorticity β of the flow. Although flow vorticity affects the time evolution of the drop shape C, D and orientation θ, the parameters C and D are identically related by the same function (3.8) during evolution.

3.3. *Short- and long-time behaviors*

We consider elongation of an initially spherical drop ($C = D = 1$ at time $t = 0$). In figure 1, the evolution of the drop shape is plotted from numerical integration of equation (3.7)

† We use here symbols C for the axis ratio, and $\mathbf{C}$ for the fourth-order tensor, to follow Wetzel & Tucker (2001). No confusion should be made between the two quantities.

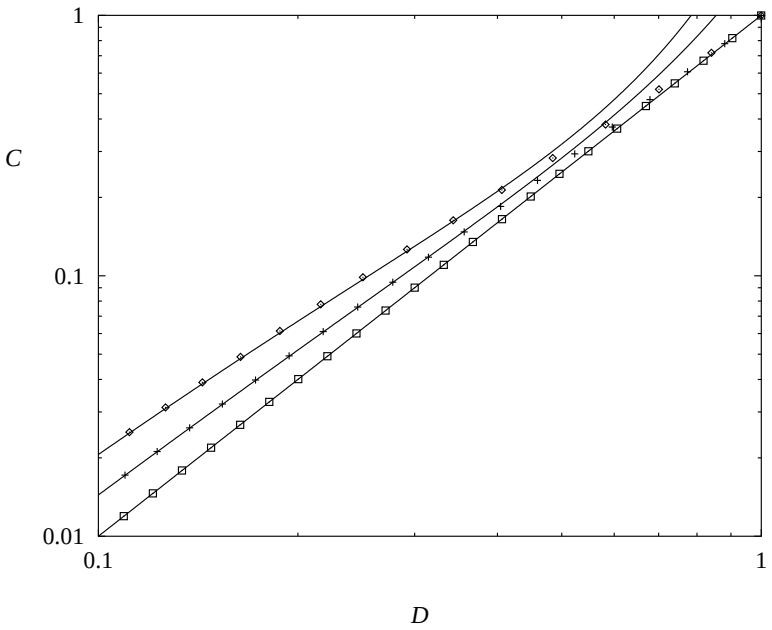

FIGURE 1. Axis ratios C and D during drop elongation from spherical ($C = D = 1$), for $Ca \to \infty$. Numerical integration of (3.7) for $\lambda = 0$ (diamonds), $\lambda = 0.5$ (crosses), $\lambda = 1$ (squares). Asymptotic solution (3.12) for $C, D \to 0$ (solid lines). The results shown are independent of the dimensionless vorticity β.

for several values of the viscosity ratio $\lambda \leq 1$. Drop deformation does not depend on rigid-body rotation therefore the results shown hold for arbitrary β. Drop widening implies $R_1 > R_3 > R_2$ or, equivalently, in terms of the axis ratios,

$$C < D < 1 \quad \text{at} \quad t > 0.$$

For $\lambda = 1$, the affine shape

$$C = D^2 \tag{3.9}$$

holds identically at $t \geq 0$ (corresponding to the slope=2 in the log-log plot), as can be easily derived from equation (3.7), which, using the definitions for the B^*_{ij} provided by Wetzel & Tucker (2001), becomes $(D/C)\ \mathrm{d}C/\mathrm{d}D = 2$, leading to (3.9). Note that equation (3.9) is equivalent to

$$R_1/R_0 = (R_2/R_0)^{-1}, \qquad R_3 = R_0. \tag{3.10}$$

For all values of λ the affine shape (3.9) also holds at short times ($C, D \approx 1$ at $t \approx 0$), because the drop is merely convected by the flow. Note that in contrast the history of deformation depends on λ (Wetzel & Tucker 2001) even at the initial stages of elongation; the history of deformation is investigated in §5.2.

At long times, numerical integration of (3.1) reveals that for $\lambda \leq 1$ the ellipsoidal drop becomes flattened and elongation is unbounded:

$$C, D \to 0 \quad \text{as} \quad t \to \infty. \tag{3.11}$$

Note that for $\lambda > 1$, equation (3.7) still describes the universal drop shape, but behavior (3.11) may not hold at long times. It is known for example that oscillations of drop

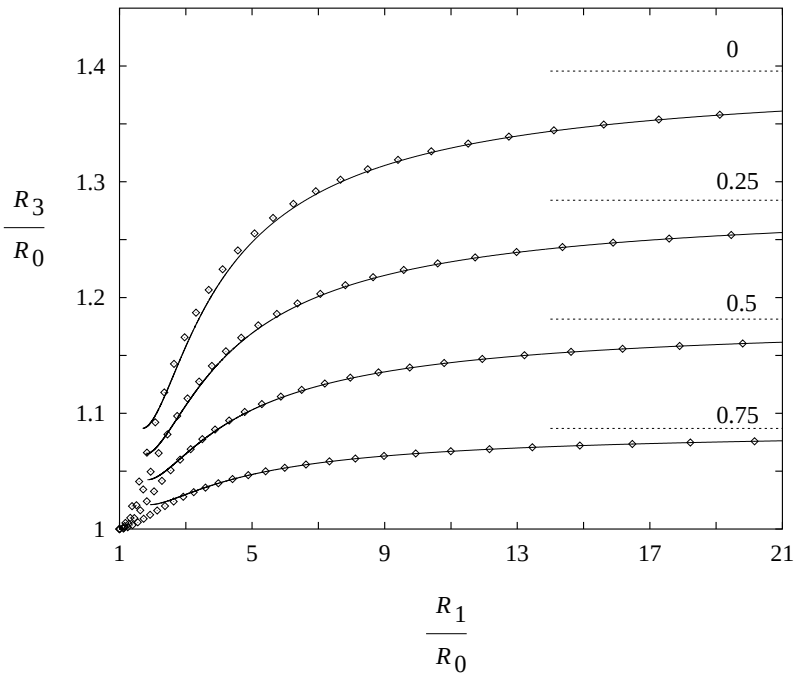

FIGURE 2. Drop width R_3/R_0 as a function of drop length R_1/R_0 during drop elongation from spherical ($C = D = 1$), for $Ca \to \infty$ and several values of λ (labelled). Numerical integration of (3.7) (diamonds), asymptotic expansion (3.12) (solid lines). The results shown hold independently of the dimensionless vorticity β. The values of width at infinity (dotted lines) are $c(0) \approx 1.395$, $c(0.25) \approx 1.284$, $c(0.5) \approx 1.181$, $c(0.75) \approx 1.087$.

shape and orientation may occur (Wetzel & Tucker 2001). To investigate the long-time behavior, we performed a Taylor series expansion of (3.7), valid for $C < D \ll 1$. This leads to the following asymptotic solution:

$$f(C, D, \lambda) = \log\left(c(\lambda)^3 D^2/C\right) - 3(1-\lambda)D \cdot (1-D) + O(D^3), \tag{3.12}$$

which is a parametric equation in $c(\lambda)$, that describes drop deformation at long times for $\lambda \leq 1$. The constant parameter $c(\lambda)$ is independent of the flow type β and is a function of the viscosity ratio λ only. Equation (3.12) has the leading behavior

$$C = c(\lambda)^3 D^2. \tag{3.13}$$

From conservation of volume, definitions (3.3), and (3.13), it follows that

$$R_3/R_0 \to c(\lambda), \quad \text{as } t \to \infty. \tag{3.14}$$

Therefore in the absence of interfacial tension drop width tends to a constant value $c(\lambda)$ at long times. The width $c(\lambda)$ at infinity cannot be calculated from our asymptotic expansion, and is obtained from numerical integration of (3.7). For $\lambda = 1$, from (3.9) and (3.13) we conclude that $c(1) = 1$. For $\lambda < 1$, numerical integration reveals that $c(\lambda) > 1$ and monotonically increases as $\lambda \to 0$, and $c(0) \approx 1.4$ (cfr. figure 10 and related discussion, where $c(\lambda)$ is plotted together with boundary-integral results for finite Ca). From (3.14) it follows that in the absence of interfacial tension the scaling (2.5) holds identically as $t \to \infty$, leading to the development of a stable lamellar microstructure.

In figure 1, expansion (3.12) is compared to numerical integration of the exact equation (3.7), revealing close agreement for $C, D \ll 1$. The evolution of drop width is illustrated in figure 2 for several values of λ from numerical integration of (3.7), and compared to the asymptotic expansion (3.12).

4. Method

4.1. *Experimental*

4.1.1. *Fluids*

The system selected for the experiments is silicone oil (SI) in polybutene (PB). The former was obtained from Dow Corning (trade name: silicone fluid 200/60,000 cSt), the latter from Exxon (trade name: Hyvis 200). Both polymers are transparent and liquid at room temperature.

Rheological characterization, including creep and oscillatory tests, was performed at several temperatures from 20 to 30 °C by using a constant stress rheometer (DSR 200, from Rheometrics Scientific). In the shear rate range investigated ($\dot{\gamma} = 0.05$—$5\ \mathrm{s}^{-1}$, with an error $\approx 2 - 3\%$), both polymers showed Newtonian behavior: viscosity was constant with shear rate and the value of storage modulus G' at $\dot{\gamma} = 1\mathrm{s}^{-1}$ was very low with respect to G''. In all the experiments the shear rate was kept well below $5\ \mathrm{s}^{-1}$ to stay within the Newtonian plateau. For higher accuracy, viscosity was also measured by using glass viscometers (Cannon) immersed in a water bath for temperature control (± 0.1°C). Care was taken to ensure that the shear rate at the capillary wall was within the Newtonian plateau. To convert the kinematic viscosity obtained by the glass viscometers into dynamic viscosity the density of the two polymers was measured by means of ASTM glass thermohydrometers (Kessler Instruments) and was $\hat{\rho} = 0.9735\mathrm{kg/m}^3$ for SI and $\rho = 0.9075\mathrm{kg/m}^3$ for PB (both data at 23°C). The resulting values of viscosity at 23°C were $\hat{\mu} = 59.3$Pa s for SI and $\mu = 638$Pa s for PB, with an error $\approx 2 - 3\%$.

The interfacial tension of the pair SI/PB was determined from the analysis of drop shape using small deformation theory; details of the procedure are described by Guido & Villone (1998). The result was $\sigma = 3.5 \cdot 10^{-3}\mathrm{N/m}$ at 23°C (with an error $\approx 5\%$), which is close to values reported in the literature for pairs of polymers having similar chemical structure (e.g., the interfacial tension of the system polyisobutylene/polydimethylsiloxane are in the range 2.5–$4 \cdot 10^{-3}\mathrm{N/m}$, depending on temperature and molecular weight (Wagner & Wolf 1993)).

It has been recently reported (Guido, Simeone & Villone 1999) that drops of polyisobutylene in polydimethylsiloxane undergo a significant shrinkage with time, which is associated with an increase of both the interfacial tension and the viscosity ratio. To evaluate the extent of such effects for drops of SI in PB, drop size was monitored with time. No significant variations were observed in the course of the experiments (which lasted a few hours), thus ensuring that the viscosity ratio is close to the value calculated from the viscosities of the pure components:

$$\lambda \approx 0.1.$$

4.1.2. *Apparatus*

The shear device used in this work is a parallel plate apparatus, which has been described in detail elsewhere (Guido & Villone 1998; Guido & Simeone 1998). Briefly, simple shear flow ($\beta = 1$) is generated by translating one plate with respect to the other by means of a computer-controlled stepper motor. Parallelism between the plates is adjusted with the aid of a set of micrometric tilting, rotary and translating stages

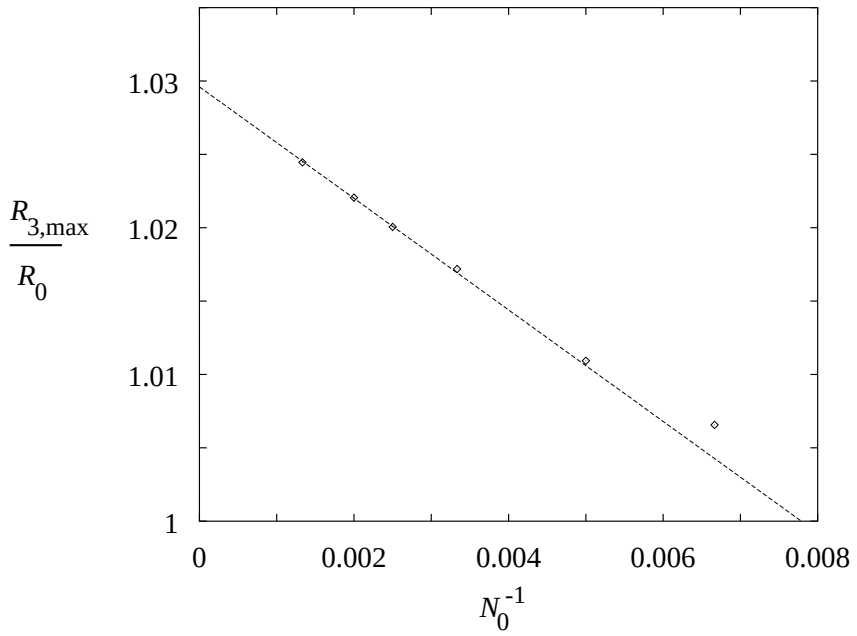

FIGURE 3. Maximum width $R_{3,\max}/R_0$ (diamonds) during drop evolution ($\beta = 0$, $\lambda = 0.5$ and $Ca = 10$) from boundary-integral simulations, as a function of initial number N_0 of grid nodes. $O(N_0^{-1})$ convergence (dashed).

with an error $\approx 20\mu$m over a length of 10 cm. Observations are performed through an optical microscope equipped with a CCD video camera and mounted on a motorized stage in order to keep the deformed drop within the field of view during shear flow. Two alternative configurations of the plates can be used to view the sample either along the vorticity (z–direction) or the velocity gradient (y–direction).

A tiny glass capillary fixed to a home made micromanipulator is used to inject a few drops of SI (of radius $R_0 = 25$—40 μm, with an error $\approx 2 - 3\%$) in the PB continuous phase, which had been previously loaded between the two plates. The rather high values of the viscosity of the selected fluids, coupled with the low difference of density, ensured that buoyancy effects were negligible for the injected drops. The distance between the parallel plates was adjusted to $\approx$1 mm to minimize wall effects.

All the experiments were carried out in a room kept at 23°C and the actual temperature of the sample was monitored by a fine gauge thermocouple directly immersed in the continuous phase (the measured temperature was 23 $\pm$0.5°C).

Images of the deforming drop were digitized by means of a frame-grabber installed on a Pentium III-based host computer, and drop contour was extracted by image analysis techniques. The two axes R_1 and either R_2 or R_3 (depending on the view) were either taken as the axes of an equivalent ellipse (i.e., having the same first and second moments of area as the image of the drop in the plane of observation) or directly measured as minimum and maximum distance of center of area from drop contour (the difference between the two methods was within the experimental error).

4.2. *Numerical*

4.2.1. *Boundary-integral simulations*

The Stokes equations, with the boundary conditions appropriate for a fluid-fluid deformable interface S, are recast as an integral equation on S (Pozrikidis 1992; Rallison & Acrivos 1978). Accordingly, the fluid velocity $\mathbf{v}(\mathbf{x})$ at a point $\mathbf{x}$ on S is obtained by solving the equation

$$\mathbf{v}(\mathbf{x}) = \frac{2}{\lambda+1}\mathbf{v}^{\infty}(\mathbf{x}) - Ca^{-1}\frac{(4\pi)^{-1}}{\lambda+1}\int_S \mathbf{G}(\mathbf{x},\mathbf{x}')\cdot\mathbf{f}(\mathbf{x}')\,\mathrm{d}S(\mathbf{x}') + \frac{3}{2\pi}\frac{\lambda-1}{\lambda+1}\int_S (\mathbf{T}(\mathbf{x},\mathbf{x}')\cdot\mathbf{v}(\mathbf{x}'))\cdot\mathbf{n}(\mathbf{x}')\,\mathrm{d}S(\mathbf{x}'), \tag{4.1}$$

where $\mathbf{x}'$ is the integration variable. The equation has been made dimensionless using the drop radius R_0 and flow time $\tau_{\dot\gamma} = \dot\gamma^{-1}$. The incident flow $\mathbf{v}^{\infty}$ is defined in §2. The surface traction resulting from capillary pressure is

$$\mathbf{f} = 2\kappa\mathbf{n}, \tag{4.2}$$

where $\mathbf{n}$ is the outward normal vector to S, and κ is the mean curvature of the interface. The kernel functions for an unbounded fluid in (4.1) are

$$\mathbf{G} = \frac{\mathbf{I}+\hat{\mathbf{x}}\hat{\mathbf{x}}}{r}, \qquad \mathbf{T} = \frac{\hat{\mathbf{x}}\hat{\mathbf{x}}\hat{\mathbf{x}}}{r^2}, \tag{4.3}$$

where $r = |\mathbf{x}'-\mathbf{x}|$ and $\hat{\mathbf{x}} = (\mathbf{x}'-\mathbf{x})/r$.

Equation (4.1) was solved numerically on a set of N interfacial marker points. An unstructured triangulated grid was used to describe the drop surface. For efficient trapezoid-rule integration the equation was transformed into a singularity-subtracted form (Loewenberg & Hinch 1996) and solved by Jacobi iteration after purging eigensolutions corresponding to $\lambda = 0$ and $\lambda \to \infty$ (Pozrikidis 1992). The normal vector and curvature were calculated either by a local surface-fitting algorithm (Zinchenko, Rother & Davis 1997) or by the line-integral method (Lowenberg & Hinch 1996). The time-step was set by a convective-stability constraint (Rallison & Acrivos 1978).

Our simulations rely on a recently-developed adaptive surface discretization algorithm that enables detailed and efficient simulations of large drop deformation (Cristini, Bławzdziewicz & Loewenberg 1998, 2001). Nearly equilateral triangulation and optimal marker-point density (proportional to κ^2) are maintained throughout the simulation. As a drop shape evolves, the number of marker points N varies in order to resolve the interface with prescribed accuracy. The accuracy is thus set by the number of marker points N_0 used to discretize the initial spherical drop shape.

4.2.2. *Computational accuracy and efficiency*

In figure 3, a convergence test for our boundary-integral simulations is shown. The numerical results for maximum drop widening $R_{3,\max}/R_0$ during evolution are reported corresponding to several mesh resolutions set by the initial number N_0 of mesh nodes. The results indicate that our simulations are $O(N_0^{-1})$ convergent; the convergence rate was found to be always negative (deformation R_3/R_0 is underestimated) and weakly dependent on the microphysical parameters. The simulations presented in this paper correspond to $N_0 = 200$ (unless otherwise stated), and have about 2% error (cfr. figure 3).

Very large deformations occur under the conditions studied here (cfr. figure 5); the most expensive boundary-integral simulations took several weeks of CPU-time on an ORIGIN

2000 workstation at the University of Minnesota Supercomputer Institute using a single processor and 400 MB of memory. Corresponding to $N_0 = 200$, the largest deformations achieved ($R_1/R_0 \approx 10$) required the final drop surface to be discretized with up to $N \approx 20,000$ nodes.

FIGURE 4. Drop configurations (next page) during evolution from two experiments in shear flow ($\beta = 1$, $\lambda = 0.1$). Left: $Ca = 9.6$, view along the gradient (negative y–direction); see figure 6. Right: $Ca = 9.1$, view along vorticity (negative z–direction). Values of strain $\dot{\gamma}t = 0$ (A,a), 1.03 (B,b), 2.22 (C,c), 4.39 (D,d). Left: drop widths $R_3/R_0 = 1$ (A), 1.03 (B), 1.113 (C), 1.028 (D).

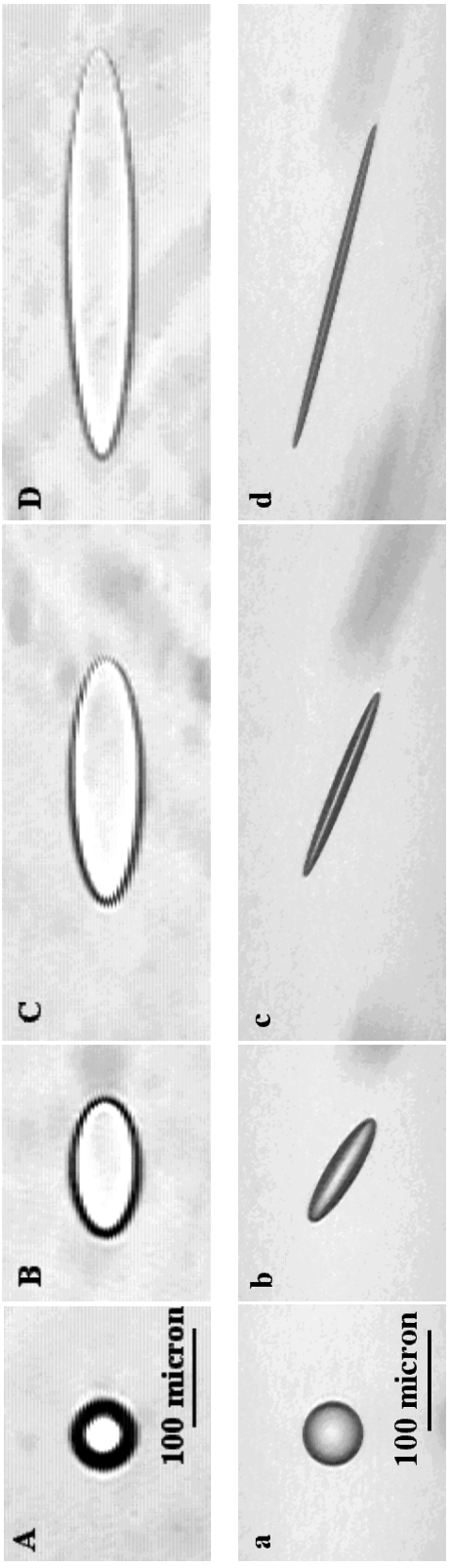
A
B
C
D
100 micron
a
b
c
d
100 micron

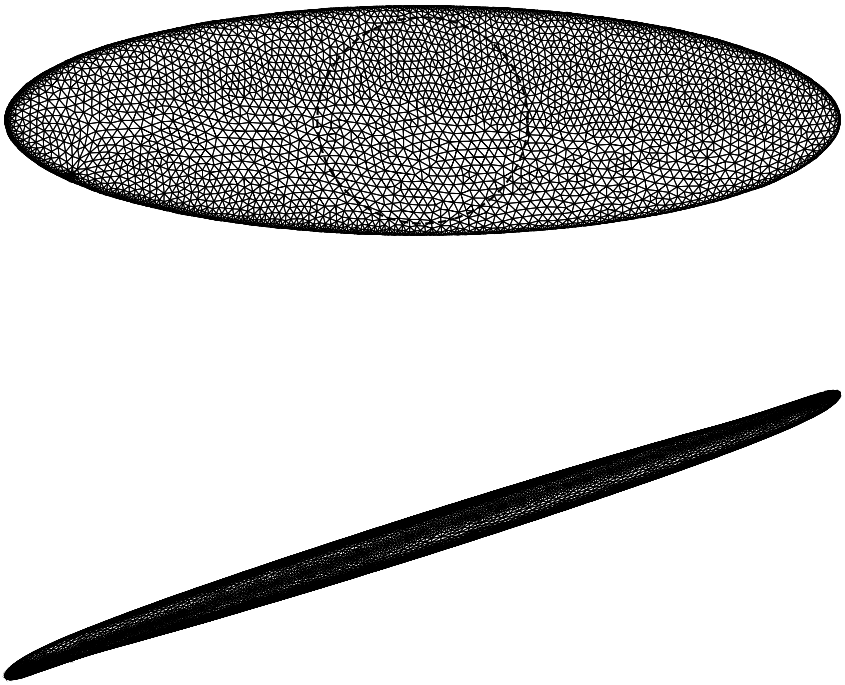

FIGURE 5. Drop configuration at maximum widening $R_{3,\max}/R_0 > 1$ during evolution in shear flow ($\beta = 1$, $\lambda = 0.1$, $Ca = 20$), from a boundary-integral simulation. Top: view along velocity gradient (y–direction); dashed circle is undeformed drop. Bottom: view along vorticity (positive z–direction). Figures 4 and 5 are not in scale.

5. Experimental and numerical results

We report in this section results for drop deformation from a spherical initial shape in a steady flow (2.1), under conditions of $\lambda \leq 1$ and finite Ca.

5.1. *Drop configurations*

Starting from rest conditions, shear flow ($\beta = 1$) was generated in our experimental apparatus by sending via serial interface to the motor controller the desired speed and number of steps of the moving plate. Once the motor stopped, the deformed drop was allowed to relax back to the spherical shape before starting a new run. The range of capillary numbers explored was $0.8 \leq Ca \leq 14.1$. The experimental data presented here and in §5.2 refer to four runs at $Ca = 2.7$, 4.6, 9.1 and 9.6 (corresponding to shear rates $\dot{\gamma} = 0.38$, 0.66, 1.33 and 1.4 s^{-1}). Drop radius was $R_0 = 39\mu$m and the distance between the parallel plates was 1500 μm. The time interval between two consecutive images is 1/25 seconds, except for the last points of the run at $Ca = 9.6$, which were taken manually at a lower rate due to the poor contrast of drop contour at high extensions (see figure 4). The lower image quality in figure 4 (left) is due to the fact that the same degree of video-enhancement was used for the drop images throughout the whole experiment. Strong video-enhancement was necessary in order to capture the details of the drop contour in the late stages of deformation, when the drop is tilted and strongly flattened and thus difficult to keep on focus.

Snap-shots of drop configurations corresponding to evolution for $Ca = 9.6$ (left) and

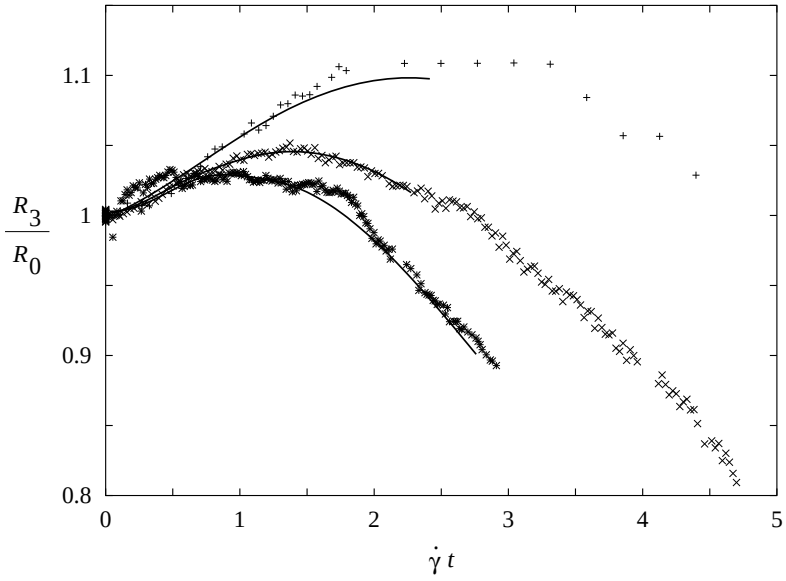

FIGURE 6. Drop width R_3/R_0 as a function of strain $\dot{\gamma}t$ in shear flow ($\beta = 1$, $\lambda = 0.1$). Experiments for $Ca = 2.7$ (*), 4.6 (x) and 9.6 (+). Converged boundary-integral simulations (solid lines) for $Ca = 3$, 5, and 10.5.

9.1 (right) are shown in figure 4. The views are in the direction of the velocity gradient and vorticity respectively. Drop widening $R_3/R_0 > 1$ and large surface area generation are evident in the third and fourth frames (left). Correspondingly, the drops are strongly flattened ($R_3 \gg R_2$) by the compressional component of the flow along the axis $y = -x$ (right). In our experiments the onset of lamellar morphology can be observed. We were not able to continue the observations beyond strains $\dot{\gamma}t \approx 5$. Note that in shear flow the drop is tilted with respect to the gradient direction, thus the corresponding images (left) in figure 4 are of the projection of the area R_1R_3 onto the xz plane.

These features can also be observed in figure 5, where drop configurations during evolution in shear flow are depicted from a boundary-integral simulation. The figure corresponds to the maximum extent of widening $R_{3,\max}/R_0$ during the evolution (cfr. figures 6 and 7), when local surface-tension effects become important (as revealed in figure 5 for the view along the vorticity by the bent shape of the drop tips). Here, a higher capillary number than in figure 4 was chosen to emphasize the widening of the shape.

5.2. *Transient deformation*

In figure 6, the time evolution of the drop width R_3/R_0 is reported from three experiments (the view was along the velocity gradient, y–direction, so that drop width could be measured). Drop width increases and reaches a maximum, when local surface tension becomes important, causing the width to decrease. Thus, for finite surface tension (finite Ca), drop widening and the development of a lamellar morphology described by the scaling (2.5) are transient phenomenona. Corresponding to higher capillary numbers, the extent of widening is larger, and drops maintain an $O(1)$ width for longer times. As indicated by the negative slopes at large strains in figure 6, the drop width will decrease

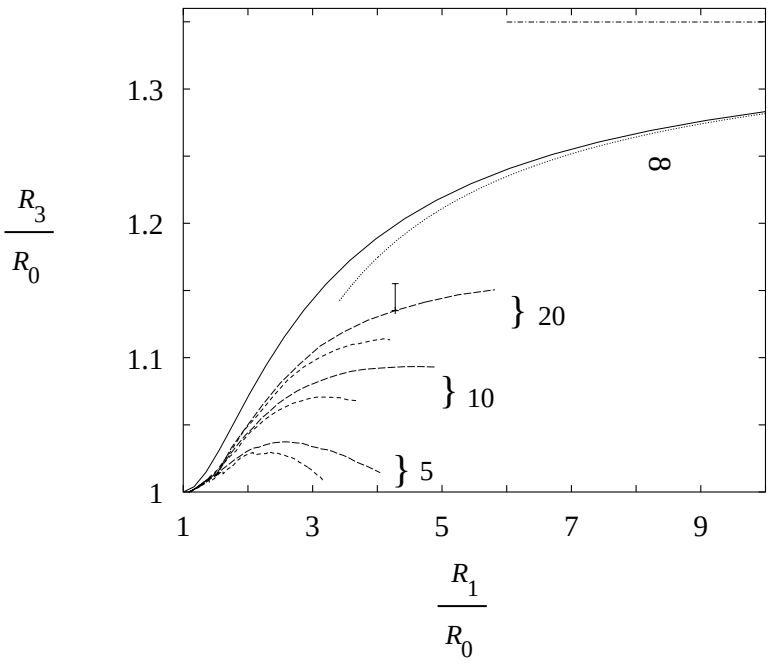

FIGURE 7. Width R_3/R_0 as a function of length R_1/R_0, during drop evolution for $\lambda = 0.1$, Ca labeled. Boundary-integral simulations: $\beta = 0$ (long dashed), $\beta = 1$ (short dashed); herein, one error bar applies to all boundary-integral curves (see §4.2.2). Numerical integration of equation (3.7) for $Ca \to \infty$, valid for all β, (solid), with limiting width $c(0.1) \approx 1.35$ (dashed-dotted). Long-time solution (3.12) of equation (3.7) (dotted).

as it continues to lengthen, and a round neck will eventually form that thins according to the scalings of (2.6). Drop elongation and thinning will continue until breakup (Marks 1999; Cristini *et al.* 2001; Renardy & Cristini 2001a,b). In figure 6 the experimental observations are compared to boundary-integral simulations converged to $O(N_0^{-2})$ accuracy by extrapolating numerical results corresponding to several values of N_0 to $N_0 \to \infty$, as described in §4.2.2. In the simulations, the capillary numbers were reset by $\approx 10\%$ to account for the uncertainty in the experimental parameters. The comparison with the numerical results reveals good agreement, and supports the estimates for the experimental errors given in §4.1. Even for $Ca = 9.6$ the discrepancy is within the scatter of the experimental points. The drop configurations during evolution are strongly deformed and flattened (see figures 4 and 5); due to computational expense, the simulations could be continued up to the end of the experimental data in figure 6 only for the lowest capillary number examined.

Drop width is shown in figure 7 as a function of drop length during evolution in hyperbolic ($\beta = 0$) and shear ($\beta = 1$) flows as determined from boundary-integral simulations for one value of viscosity ratio $\lambda = 0.1$. The curve in figure 7 for $Ca \to \infty$ represents the universal behavior independent of flow type β as discussed in §3 (see figure 2). For finite capillary numbers, small deviations from the spherical shape are unaffected by surface tension, and the shape is equal to the affine shape (3.9), with no β-dependence (the difference visible in the figure between the results at small deformations is within the numerical error indicated by the error-bar). However, the maximum extent of drop

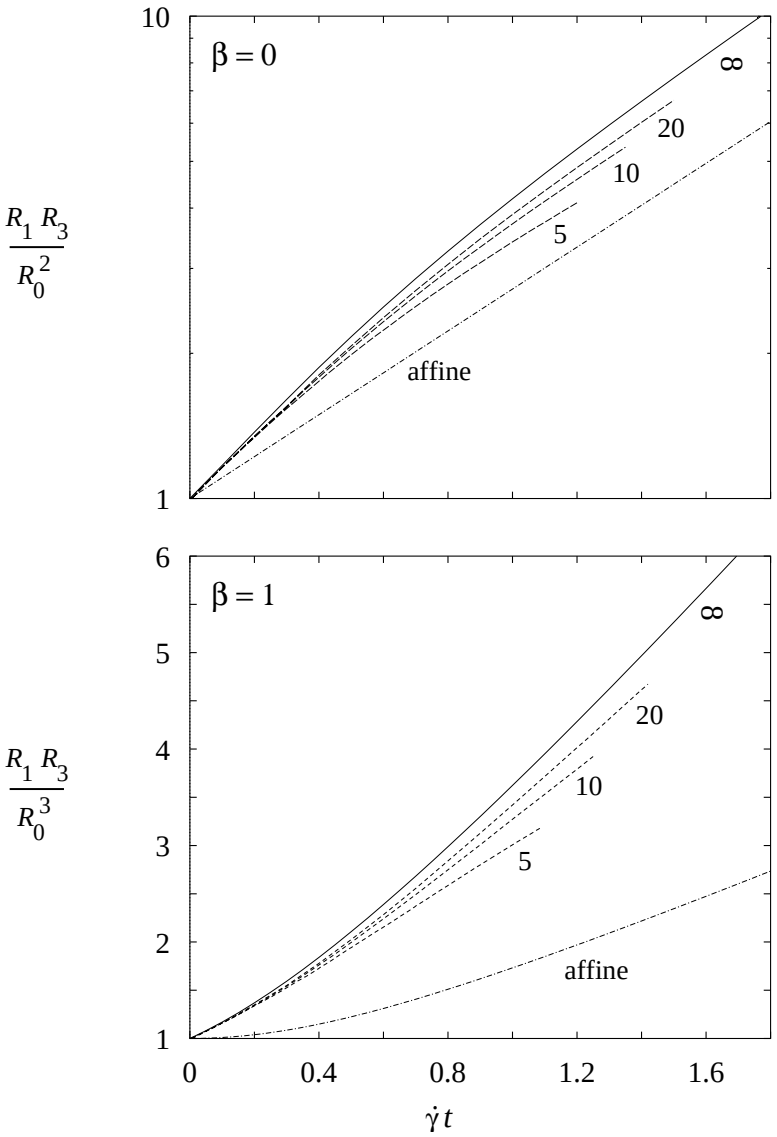

FIGURE 8. Area generation $R_1 R_3 / R_0^2$ as a function of strain $\dot{\gamma} t$, during evolution for $\lambda = 0.1$ and Ca labeled. Top: $\beta = 0$ (semi-log scale); bottom: $\beta = 1$. Solid, long- and short-dashed as in figure 7. Affine deformation: $\lambda = 1$, $Ca \to \infty$ (dashed-dotted), from numerical integration of (3.1). For affine evolution, area generation is linear (at long times) in shear flow, and exponential in hyperbolic flow.

widening is lower in flows with more rotation. With increasing β, the drop is more effectively rotated away from the extensional axis $y = x$ of the flow thereby hindering deformation. Comparison of the results of simulations to the behavior for $Ca \to \infty$ reveals that the maximum theoretical widening $c(\lambda)$ can be approached only at very high capillary numbers and for very large strains (see figures 10 and 11).

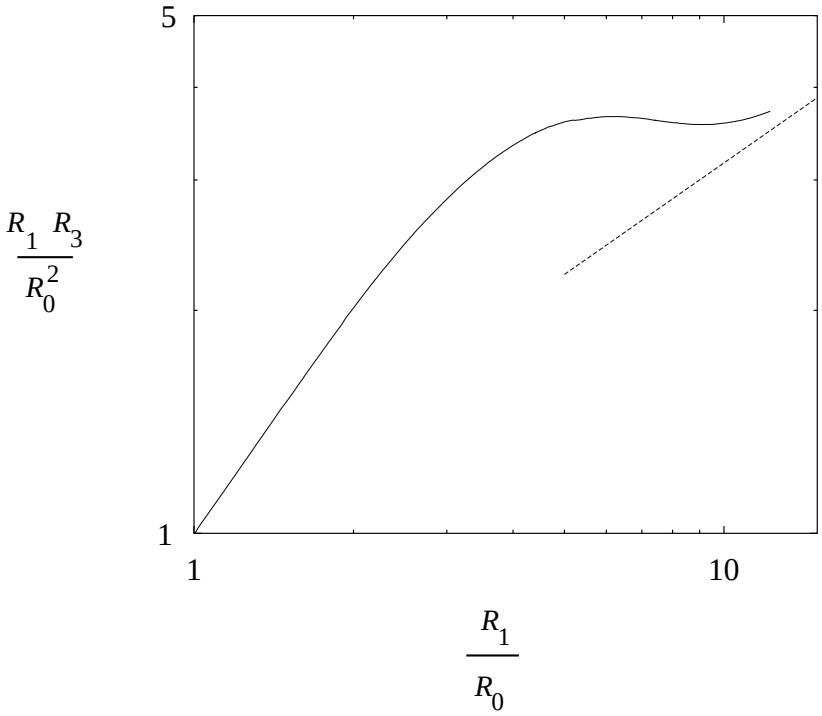

FIGURE 9. Area generation R_1R_3/R_0^2 as a function of drop length R_1/R_0 during evolution in shear flow ($\beta = 1$, $\lambda = 0.1$, $Ca = 3$), from a boundary-integral simulation. Initial slope=1 (initial evolution obeys (3.9)) and dashed line with slope=1/2 correspond to the scalings (2.5) and (2.6), respectively.

In figure 8, the area-generation history is reported for the same conditions of figure 7. Area generation is larger for higher capillary numbers, corresponding to increased drop width and length. Area generation is delayed in flows with vorticity (bottom plot). The area generation associated with widening when $\lambda < 1$ exceeds considerably the result for affine transient deformation ($\lambda = 1$, $Ca \to \infty$) for all β. The behavior illustrated in figures 7–8 is only quantitatively affected by λ.

The numerical results shown in figure 9 correspond to shear flow with the lowest capillary number examined (because of computational expense). At finite capillary numbers, area generation slows down after the maximum width is reached (this does not happen in the limit $Ca \to \infty$, because drop width R_3 is constant at long times). The development of a lamellar morphology is a transient phenomenon. Initially, the drop is flattened by the flow; widening occurs, and the area generation follows the scaling (2.5). At long times, the drop has a slender cylindrical shape because of surface tension; from conservation of mass, the area R_1R_3 follows the scaling (2.6). The scalings are supported by the numerical simulation reported in figure 9.

5.3. *Effects of flow and microphysical parameters*

In figure 10, the maximum extent of drop widening during elongation is shown as a function of the viscosity ratio λ. Several curves for different capillary numbers and flow types are reported from boundary-integral simulations. Drop widening occurs for viscosity ratios $0 \leq \lambda < 1$ because of the compressional component of the planar flow (2.1) along the direction $y = -x$. For $\lambda = 1$ and $Ca \to \infty$ affine deformation occurs, which is

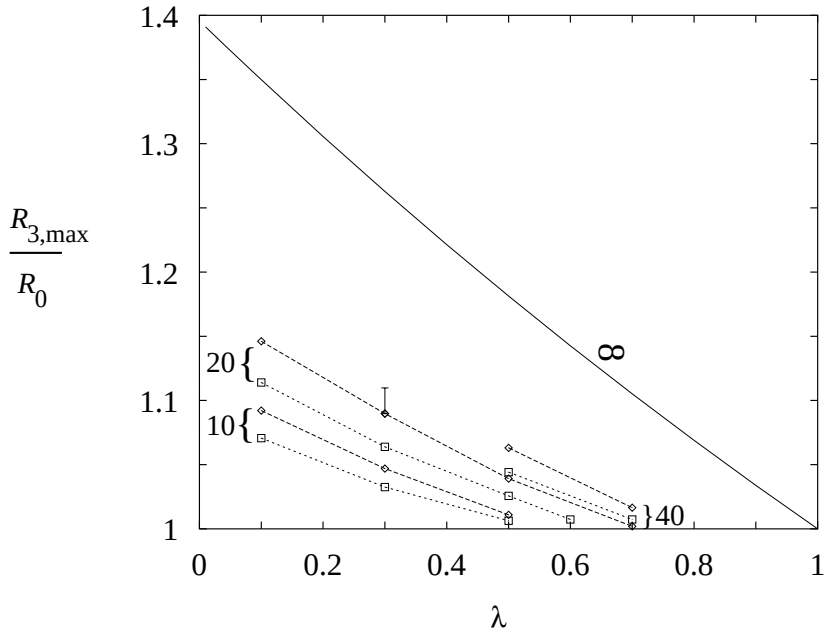

FIGURE 10. Maximum width $R_{3,\max}/R_0$ during drop evolution, as a function of viscosity ratio λ, from boundary-integral simulations for $\beta = 0$ (diamonds) and $\beta = 1$ (squares), and capillary numbers Ca labeled. Maximum theoretical widening $c(\lambda)$ defined in equation (3.12) and valid for all β, calculated from numerical integration of equation (3.7) (solid line).

incompatible with widening in the vorticity direction. The extent of widening increases (roughly linearly with λ) as $\lambda \to 0$; no viscous stresses inside the drop resist deformation under such conditions. For a given λ, the maximum widening in the limit $Ca \to \infty$ (function $c(\lambda)$ introduced in (3.12)) was determined by numerical integration of equation (3.7). Widening is largest as $Ca \to \infty$ and is independent of the flow type; i.e., at infinite capillary number rigid-body rotation only affects the time evolution (see §3 and figure 8). For finite capillary numbers drop widening increases with increasing capillary number and decreasing flow vorticity β.

The sensitivity of drop widening on Ca is illustrated in detail with an example from shear flow in figure 11. As indicated in the figure, widening tends to saturate only at very large capillary numbers $Ca \gg 10^2$. The dependence of drop widening on Ca remains qualitatively unchanged for different flow types and viscosity ratios, indicating that the effect of surface tension results in a very strong decrease in the extent of widening (and area generation). In our numerical simulations, we were unable to describe drop deformation for $Ca \to \infty$ because the extremely large strains were computationally too expensive to resolve within specified accuracy.

The results of the boundary-integral simulations reported in figure 10 reveal that there exists a capillary number $Ca_0(\lambda)$ below which no widening occurs. This minimum capillary number for widening increases with the viscosity ratio, and $Ca_0 \to \infty$ as $\lambda \to 1$. Such dependence is exemplified in table 1 for hyperbolic flow. The error-bar in figure 10 indicates that the values in table 1 are rough estimates.

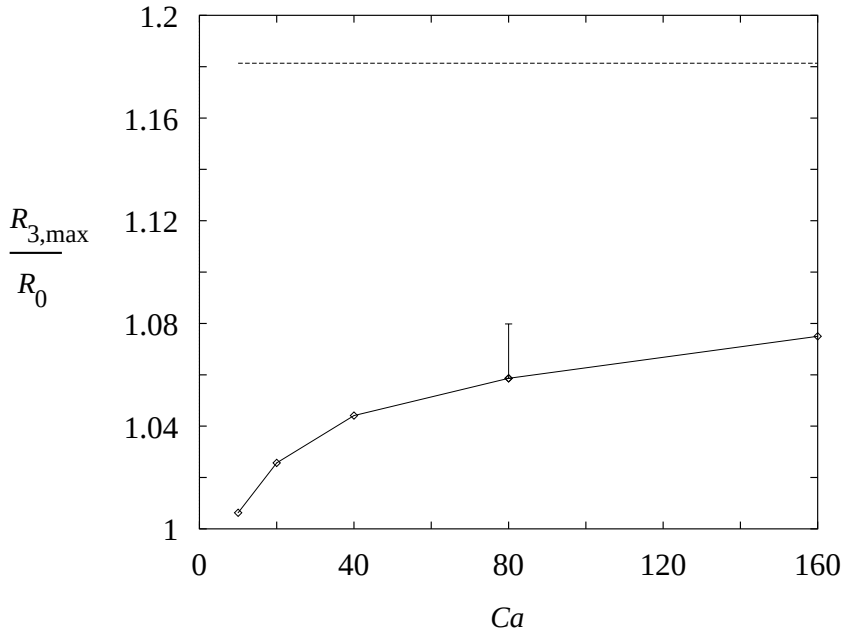

FIGURE 11. Maximum width $R_{3,\max}/R_0$ during drop evolution, as a function of capillary number Ca, from boundary-integral simulations ($\beta = 1$, $\lambda = 0.5$). Dashed line: maximum theoretical widening $c(0.5) \approx 1.181$, from numerical integration of equation (3.7).

λ	Ca_0
0.1	1
0.3	5
0.55	10
0.7	20
0.8	40

TABLE 1. Minimum capillary number Ca_0 for drop widening as a function of viscosity ratio λ, from boundary-integral simulations reported in figure 10; $\beta = 0$.

6. Conclusions

We have investigated transient drop deformation in planar flows under Stokes flow conditions and capillary numbers $Ca > 1$. A remarkable surface area generation that exceeds that of affine deformation is associated with $O(1)$ drop widening and occurs for viscosity ratios $\lambda < 1$. This mechanism is responsible for the formation of transient lamellar microstructures in emulsions. The extent of area generation is found to increase with increasing capillary number Ca and decreasing viscosity ratio λ and decreasing flow vorticity β. For finite capillary numbers, the extent of widening reaches a maximum before decreasing, as local capillary effects become important and area generation slows down. In the limit $Ca \to \infty$ drop widening remains constant as $t \to \infty$ and the lamellar morphology is stable; for zero interfacial tension, drop deformation is a universal function of λ independent of the flow type β, which merely sets the time scale for deformation. Flows without rotation correspond to the largest rates of area generation.

These results describe the onset of lamella formation in dilute Newtonian systems and thus represent a first step towards an understanding of the evolution of the microstruc-

ture in polymer blends during processing. The feasibility of accurate experiments demonstrated here for Newtonian systems with constant interfacial tension indicates that more comprehensive experimental investigations should be possible for more complex rheology and interfacial phenomena.

Preliminary experimental work showed that block and graft copolymers can increase drop deformation very significantly (Levitt 1997; Levitt & Macosko 1999; Jeon & Macosko 2000). Proposed mechanisms involve a decrease in surface tension, redistribution of surfactant towards the edges of the drop, and decreased interfacial slip (de Gennes 1989; Goveas & Fredrickson 1998; Zhao & Macosko 2001). Area generation in the presence of block copolymers is being quantitatively described via experiments by Jeon & Macosko (2000). A new, adaptive finite element numerical method that includes non-uniform surface tension is in preparation. This should help such investigations by isolating the effect of flow-driven surfactant redistribution on a drop interface.

A finite element algorithm is in preparation (Hooper *et al.* 2001) for extending the analysis to viscoelastic fluids. According to recent experimental investigations (Levitt, Macosko & Pearson 1996; Levitt 1997; Jeon & Macosko 2000), higher elasticity of the matrix fluid can considerably enhance the amount of widening and area generation under shear. Numerical simulations of the effect of elastic normal stresses on drop deformation will help the design of processing conditions leading to optimal lamellar morphology of polymeric blends.

Finally, boundary-integral simulations of concentrated emulsions under conditions for which drop deformation is large are underway. At finite volume fractions of the dispersed droplet phase, competing mechanisms involve hydrodynamic interactions along the velocity gradient and vorticity directions. Preliminary results reveal a change in the extent of drop widening and area generation.

Acknowledgments

VC, RH and CWM were supported by grant DAAD19-991-0337 from the Army Research Office. VC also acknowledges the Institute for Mathematics and its Applications for their hospitality, and the Minnesota Supercomputing Institute for a Research Scholarship, and for computing time and support. MS and SG were supported by departmental funding.

REFERENCES

Comas-Cardona, S. & Tucker, C. L. 2001 Measurements of droplet deformation in simple shear flow with zero interfacial tension. *J. Rheol.* **45**, 259–273.

Cristini, V., Bławzdziewicz, J. & Loewenberg, M. 1998 Drop breakup in three-dimensional viscous flows. *Phys. Fluids* **10**, 1781–1783.

Cristini, V., Bławzdziewicz, J. & Loewenberg, M. 2001 An adaptive mesh algorithm for evolving surfaces: simulations of drop breakup and coalescence. *J. Comput. Phys.* **168**, 445–463.

Cristini, V., Guido, S., Alfani, A., Bławzdziewicz, J. & Loewenberg, M. Drop breakup in shear flow. In preparation.

de Gennes, P. G. 1989 Adhesion of two slightly incompatible polymers. *C. R. Acad. Sci. II* **308**, 1401–1403.

Delaby, I., Ernst, B., Germain, Y. & Muller, R. 1994 Droplet deformation in polymer blends during uniaxial elongational flow: Influence of viscosity ratio for large capillary numbers. *J. Rheol.* **38**, 1705–1720.

Delaby, I., Ernst, B. & Muller, R. 1995 Drop deformation during elongational flow in

blends of viscoelastic fluids. Small deformation theory and comparison with experimental results. *Rheol. Acta* **34**, 525–533.

Garmabi, H. & Kamal, M. R. 1997 Improved barrier and mechanical properties of laminar polymer blends. *Soc. Plast. Eng. Tech. Papers (ANTEC)* **55**, 2687–2691.

Goveas, J. L. & Fredrickson, G. H. 1998 Apparent slip at a polymer-polymer interface. *European Phys. J. B.* **2**, 79–92.

Guido, S. & Simeone, M. 1998 Binary collisions of drops in simple shear flow by computer assisted video optical microscopy. *J. Fluid Mech.* **357**, 1–20.

Guido, S. & Villone, M. 1998 Three-dimensional shape of a drop under simple shear flow. *J. Rheol.* **42**, 395–415.

Guido, S., Simeone, M. & Villone, M. 1999 Diffusion effects on the interfacial tension of immiscible polymer blends. *Rheol. Acta* **38**, 287–296.

Hooper, R., Cristini, V., Shakya, S., Lowengrub, J., Macosko, C. W. & Derby, J. J. 2001 Modeling multiphase flows using a novel 3D adaptive remeshing algorithm. In "Computational Methods in Multiphase Flow," Eds.: C.A. Brebbia and H. Power, Series: Advances in Fluid Mechanics, Vol. 29, Wessex Institute of Technology Press, UK.

Jeon, H. K. & Macosko, C. W. 2000 The effect of block copolymers on droplet deformation in immiscible blends. *AIChE annual meeting, paper 134k, Los Angeles, Nov. 12–17*

Kim, S. & Karrila, S. J. (1991) *Microhydrodynamics: principles and selected applications.* Butterworth-Heinemann, London.

Lee, S.-Y. & Kim, S.-C. 1996 Morphology and oxygen barrier properties of LDPE/EVOH blends. *Intern. Polym. Process* **11**, 238–247.

Levitt, L., Macosko, C. W. & Pearson, S. D. 1996 Influence of normal stress difference on polymer drop deformation. *Polym. Eng. Sci.* **36**, 1647–1658.

Levitt, L. 1997 Area generation in two-phase polymer melt processing. PhD thesis, University of Minnesota.

Levitt, L. & Macosko, C. W. 1999 Shearing of polymer drops with interface modification. *Macromolecules* **32**, 6270–6277.

Loewenberg, M. & Hinch, E. J. 1996 Numerical simulation of a concentrated emulsion in shear flow. *J. Fluid Mech.* **321**, 395–419.

Lohfink, G. W. & Kamal, M. R. 1993 Morphology and permeability in extruded polypropylene/ethylene-vinyl alcohol copolymer blends. *Polym. Eng. Sci.* **33**, 1404–1420.

Maffettone, P. L. & Minale, M. 1998 Equation of Change for Ellipsoidal Drops in Viscous Flow. *J. Non-Newtonian Fluid. Mech.* **78**, 227–241.

Marks, C. 1999 Droplet deformation and breakup in sudden onset strong flows. PhD thesis, University of Maryland at College Park.

Pozrikidis, C. 1992 *Boundary integral and singularity methods for linearized viscous flow.* Cambridge University Press.

Rallison, J. M. & Acrivos, A. 1978 A numerical study of the deformation and burst of a drop in an extensional flow. *J. Fluid Mech.* **89**, 191–209.

Renardy, Y. & Cristini, V. 2001a Effect of inertia on drop breakup under shear. *Phys. Fluids* **13**, 7–13.

Renardy, Y. & Cristini, V. 2001b Scalings for fragments produced from drop breakup in shear flow with inertia. *Phys. Fluids* In press.

Saito, T. & Macosko, C. W. 1998 A Study of Interfacial Effect in Polymer Blends under Shear and Extensional Flow. In *Proceedings of the 14th Intl Polymer Processing Society Meeting, Yokohama June 9–12* pp. 261–262.

Sondergaard, K. & Lyngaae-Jorgenson, J. 1996 Coalescence in an interface-modified polymer blend as studied by light scattering measurements. *Polymer* **37**, 509–517.

Stone, H. A. 1994 Dynamics of drop deformation and breakup in viscous fluids. *Ann. Rev. Fluid Mech.* **26**, 65–102.

Subramanian, P. M. 1984 U.S. Patent **4**, 444,817.

Subramanian, P. M. 1985 Permeability barriers by controlled morphology of polymer blends. *Polym. Eng. Sci.* **25**, 483–487.

Subramanian, P. M. & Mehra, V. 1987 Laminar morphology in polymer blends: structure and properties. *Polym. Eng. Sci.* **27**, 663–668.

SUBRAMANIAN, P. M. & PLOTZKER, I. G. 2000 Barrier materials by blending. In *Polymer Blends* (ed. D. R. Paul & C. B. Bucknall), ch. 30, pp 359–393. Wiley, New York.

UTRACKI, L. A. 1991 *Two-phase polymer systems.* Hanser, Munich.

VINCKIER, I., MOLDENAERS, P. & MEWIS, J. 1996 Relationship between rheology and morphology of model blends in steady shear flow. *J. Rheol.* **40**, 613–631.

VINCKIER, I., MEWIS, J. & MOLDENAERS, P. 1997 Stress relaxation as a microstructural probe for immiscible polymer blends. *Rheol. Acta* **36**, 513–523.

VINCKIER, I., MOLDENAERS, P. & MEWIS, J. 1997 Transient rheological response and morphology evolution of immiscible polymer blends. *J. Rheol.* **41**, 705–718.

WAGNER, M. & WOLF, B. A. 1993 Interfacial tension between poly(isobutylene) and poly(dimethylsiloxane): influence of chain length, temperature, and solvents. *Macromolecules* **26**, 6498–6502.

WETZEL, E. D. & TUCKER, C. L. 2001 Droplet deformation in dispersions with unequal viscosities and zero interfacial tension. *J. Fluid Mech.* **426**, 199–228.

YAMANE, H., TAKAHASHI, M., HAYASHI, R., OKAMOTO, K., KASHIHARA, H. & MASUDA, T. 1998 Observation of deformation and recovery of poly(isobutylene) droplet in a poly(isobutylene)/poly(dimethyl siloxane) blend after application of step shear strain. *J. Rheol.* **42**, 567–580.

YUAN, Q., FRIEDRICH, K. & KARGER-KOCSIS, J. 1994 Relationship between microstructure and impact properties in a discontinuous microlayer polymer composite of HDPE and modified PA. *Plastic Rubber Compos. Process Appl.* **22**, 29–35.

ZHAO, R. & MACOSKO, C. W. 2001 Slip at polymer-polymer interfaces: rheological measurements on coextruded multilayers. *J. Rheol.* In review.

ZINCHENKO, A. Z., ROTHER, M. A. & DAVIS, R. H. 1997 A novel boundary-integral algorithm for viscous interaction of deformable drops. *Phys. Fluids A* **9**, 1493–1511.